Catalysis Science & Technology

Structure Sensitivity in Pt-Catalyzed Hydrodeoxygenation of Multi-Oxygenated Lignol Model Compounds

Journal:	*Catalysis Science & Technology*
Manuscript ID	CY-ART-05-2023-000757.R1
Article Type:	Paper
Date Submitted by the Author:	18-Aug-2023
Complete List of Authors:	Marlowe, Justin; University of California Santa Barbara Ford, Peter; University of California, Santa Barbara, Department of Chemistry and Biochemistry Abu-Omar, Mahdi; University of California, Santa Barbara, Department of Chemistry and Biochemistry Christopher, Phillip; University of California Santa Barbara,

ARTICLE

Structure Sensitivity in Pt-Catalyzed Hydrodeoxygenation of Multi-Oxygenated Lignol Model Compounds

Received 00th January 20xx,
Accepted 00th January 20xx

DOI: 10.1039/x0xx00000x

Justin Marlowe,[a] Peter C. Ford,[b] Mahdi M. Abu-Omar *[ab] and Phillip Christopher *[a]

The valorization of lignin into aromatic chemicals such as benzene, toluene, and xylenes (BTX) has the potential to promote sustainability in the chemical industry. A critical step in this valorization is the removal of oxygen atoms from lignin-derived substrates by hydrodeoxygenation (HDO), typically catalyzed by supported metal catalysts. However, the structure sensitivity of supported metal catalysts for HDO has been under-explored, particularly for Pt catalysts and multi-oxygenated substrates that are representative compounds for realistic lignin/lignol feedstocks. In this work, the structure sensitivity of Pt catalysts supported on inert SiO_2 for the HDO of dihydroeugenol (DHE), exhibiting both hydroxy and methoxy functionalities, is explored by varying the Pt particle size distribution, and thus the fraction of exposed well-coordinated and under-coordinated Pt active sites. The desired HDO reactions are removal of methoxy substituents (partial HDO) and phenolic OH (complete HDO), while avoiding aromatic hydrogenation leading to undesired saturated hydrocarbons. Measurements of Pt particle size dependent reactivity demonstrate that aromatic ring hydrogenation is more effectively catalyzed by well-coordinated Pt sites located on low-index planes of Pt nanoparticles, which become the dominant exposed active site with Pt particle sizes above ~4 nm. Pt nanoparticles of ~2 nm exhibit high selectivity toward partial HDO via demethoxylation, forming of 4-propylphenol without significant aromatic ring hydrogenation. Interestingly, our results suggest well-coordinated Pt sites also facilitate surface tautomerization of phenol to the keto form (dienone), which is essential for complete HDO via dehydroxylation over supported metals on non-acidic supports under mild conditions (<300˚C). These findings identify a trade-off exhibited by Pt catalysts in the HDO of lignols, wherein well-coordinated Pt sites promote both complete HDO to aromatics as well as aromatic hydrogenation, while Pt catalysts exhibiting primarily under-coordinated sites selectively produce partial HDO products (i.e. phenols). The mechnanistic implications related to these observations are discussed.

Introduction

Lignocellulosic biomass is a candidate feedstock for manufacturing sustainable chemicals and fuels considering its abundance, renewability, and non-edible composition[1]. Of particular interest is the valorization of lignin, which today finds limited use as a combustible fuel for industrial energy and heat generation, despite being the largest natural source of aromatics[2,3]. Aromatic hydrocarbons, such as benzene, toluene, and xylene (BTX), are essential precursors to the production of plastics, resins, and other commodity chemicals generating over USD $100 billion annually[4,5]. Realization of chemistries that valorize lignin and lignol molecules into BTX-type products would validate renewable feedstocks and reduce carbon emissions associated with the production of aromatics and their derivatives[6,7].

Chemical conversion processes such as pyrolysis (catalytic[8,9] and non-catalytic[10,11]) and reductive catalytic fractionation[12–14] produce heterogeneous mixtures of phenolic monomers from lignin that require subsequent removal of oxygen down to parts-per-million levels to replace current BTX feedstocks. The most promising approach for oxygen removal is catalytic hydrodeoxygenation (HDO), which typically employs transition or noble metal nanoparticles on oxide, carbon, or zeolite supports. Carbide[15–17] and phosphide[18–20] catalysts have also been explored. The most active catalysts are metal nanoparticles known also to be active hydrogenation catalysts (Ni, Pt, Ru, etc.) supported on acidic oxides or zeolites[21–27]. However, these catalysts exhibit shortcomings, including deactivation by coking[28–30] and high selectivity to fully hydrogenated alkane products[31,32]. Hydrogenation of the aromatic ring during HDO results in excess H_2 consumption and the production of saturated hydrocarbon products with lower value than aromatics. The trade-off between HDO reactivity and aromatic ring hydrogenation make it desirable to find catalysts that exhibit high selectivity for HDO towards deoxygenated aromatic products without sacrificing overall activity.

Multiple approaches have been reported for improving aromatic selectivity in catalytic HDO processes, such as using reducible oxides as catalysts in the absence of a hydrogenation

[a] Department of Chemical Engineering, University of California Santa Barbara, Santa Barbara, California 93106, USA. E-mail: pchristopher@ucsb.edu, abuomar@chem.ucsb.edu
[b] Department of Chemistry and Biochemistry, University of California, Santa Barbara, Santa Barbara, California 93106, USA.
†Electronic Supplementary Information (ESI) available: See DOI: 10.1039/x0xx00000x

metal (i.e. MoO_3 without Pt[33,34]) or the use of low, even ambient[35–37], H_2 pressures. These approaches require higher temperatures and result in lower rates than catalysts based on hydrogenation metals at high H_2 pressures. Both of these approaches attempt to improve HDO selectivity by specifically targeting a decrease in the rate of hydrogenation in the multi-step HDO pathway, either by eliminating stable adsorption sites for hydrogen or by limiting the coverage of hydrogen on the metal. However, a catalyst which could afford reduced rates of hydrogenation without sacrificing overall HDO activity would be ideal.

An approach that might afford high selectivity to aromatics even under mild temperatures and high H_2 pressures is the alteration of metal nanoparticle size. It is known that aromatic ring hydrogenation requires a planar adsorption geometry that has a relatively large ensemble requirement (~6 Pt atoms[38–40]) compared to the activation of other moieties, a requirement that makes it sensitive to changes in particle size and shape. Metal particle size-dependent reactivity derives from the decreasing relative concentrations of extended metal terraces (well-coordinated, flat surfaces) with decreasing particle size and the concomitant increase in relative concentration of under-coordinated metal sites (steps, edges, corners, etc.). The sensitivity of catalytic reactivity to particle size has been observed in benzene hydrogenation over Pt/SiO_2 catalysts, where smaller Pt nanoparticles exhibited lower turnover frequencies for hydrogenation to cyclohexane than larger particles, demonstrating the importance of extended flat metal surfaces for ring hydrogenation[41]. Therefore, our premise is that the use of small metal nanoparticles in HDO reactions might restrict planar aromatic ring adsorption, thus improving selectivity towards aromatic products.

Interestingly, the opposite trend has been observed for deoxygenation turnover frequency, which increases on smaller metal particles, stemming from facilitated C-O cleavage at undercoordinated sites on metal nanoparticle surfaces[42–44], which increase in relative content with decreasing particle size. Thus, smaller metal particle sizes might suppress planar adsorption of phenolics, resulting in decreased rates of hydrogenation, but facilitate the cleavage of C-O bonds at under-coordinated sites with a high capacity for deoxygenation. Importantly, however, it has been shown that this trend in deoxygenation activity breaks down at the single atom limit[45], potentially due to insufficiently small ensemble size and accessible charge states for C-O bond cleavage. Thus, it is reasonable to expect that an optimum metal particle size may exist that maximizes HDO activity and selectivity.

Despite the evidenced influence of metal particle size (and active site structure) on reactions associated with HDO of lignin-derived monomers, limited work exists that tests this hypothesis. For example, it was found that in phenol HDO, turnover frequencies for hydrogenation increased and deoxygenation decreased with increasing particle sizes between 5 and 22 nm over Ni/SiO_2 catalysts[46]. Similarly, it was demonstrated for HDO of m-cresol over Ni/SiO_2 catalysts that smaller Ni particle sizes suppressed methanation via hydrogenolysis and increased rates of HDO towards toluene[47]. However, this work also reported the increase of aromatic ring hydrogenation rates with decreasing Ni particle size, in opposition to the report on phenol HDO. These reports generally support the expected influence of metal particle size described above with regards to deoxygenation, though questions remain as to the influence of particle size on aromatic HDO product selectivity, specifically regarding the structure sensitivity of aromatic ring hydrogenation. Additionally, no investigation into the influence of metal particle size has yet been made for Pt catalysts in HDO, despite their frequent use.

Importantly, prior reports that have examined metal particle size-dependent HDO reactivity have been limited to simple mono-oxygenated substrates, such as phenol or cresol. Though these substrates provide insight into mechanistic details, realistic lignin-derived feedstocks contain a significant fraction of di- and tri-oxygenated phenolic species, consisting of both hydroxyl and alkoxyl functionalities[9,10]. As a result, there is little understanding of how metal nanoparticle size, and thus active site structure, influences HDO rates of various oxygenate functionalities (i.e. hydroxyl vs. alkoxyl group deoxygenation) and aromatic hydrogenation in multi-oxygenated phenolics.

Here we address these knowledge gaps and examine the influence Pt particle size (2- 12 nm) on the HDO of a multi-oxygenated phenolic substrate, dihydroeugenol (DHE). Pt particles were supported on SiO_2 supports to remove the influence of support acidity, and the Pt structure and exposed Pt site characteristics were characterized via transmission electron microscopy, volumetric chemisorption, and CO probe molecule FT-IR spectroscopy. Batch reactor DHE HDO studies were conducted to investigate the effects of Pt particle size on hydroxyl and methoxyl group deoxygenation, as well as aromatic hydrogenation. By measuring product concentrations as a function of substrate conversion, starting from both DHE and 4-propylphenol (Scheme 1), the influence of Pt size, and thus active site structure, on specific steps within the HDO network was elucidated. We also explore the competing roles of kinetics and thermodynamics on the product evolution in batch reactors as a function of time, driven in part by the lower hydrogen availability in liquid-phase systems compared to studies reported in the vapor phase. The findings presented here demonstrate the importance of controlling the structure

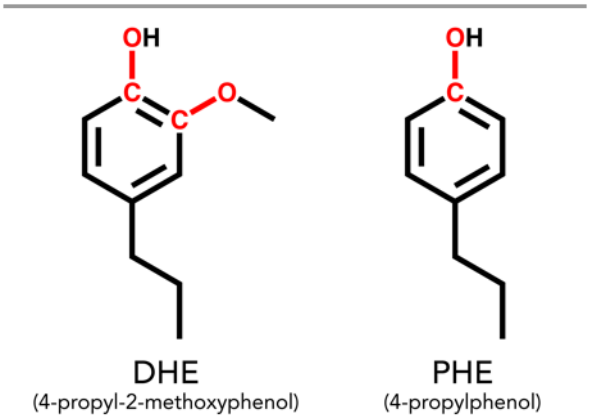

Scheme 1 Structures of model lignols utilized this work as substrates for HDO reactions.

of metal active sites to dictate desired product selectivity in the HDO of multi-oxygenated phenolics.

Methods and Materials

Catalyst Preparation

Supported Pt/SiO_2 catalysts of varying average particle size were prepared by a modified strong electrostatic adsorption (SEA) procedure using tetraamine platinum nitrate (TAPN, Sigma)[48,49]. In the case of 0.4wt% and 2wt% Pt/SiO_2 catalysts, amorphous SiO_2 (20-30 nm, USNano) was introduced to HPLC-grade water (Sigma) under magnetic stirring. The pH of the solution was adjusted to 10.5 using an appropriate amount of aqueous NH_4OH (28%, Sigma), determined by monitoring with a pH meter and probe. Once the desired pH was achieved, the solution was left stirring for 30 minutes for the SiO_2 surface to equilibrate with the solution. To this, 50 mL of TAPN in HPLC-grade water, also adjusted to pH of 10.5, was added dropwise via a syringe pump at a rate of 2.5 mL/min. After addition was complete, the solution was heated to 80˚C and allowed to evaporate under stirring. The obtained powder was then thoroughly dried overnight in an oven at 110˚C and removed.

Synthesis of the 6% Pt/SiO_2 followed a similar procedure. The SiO_2 used for this catalyst series was a non-porous SiO_2 (15-20 nm, USNano) in order to avoid Pt deposition in small pores which might stabilize small particles even under harsh calcination conditions. This SiO_2 was added to pH-adjusted water at 10.5 in a similar approach to the other catalyst preparation. To this, 10 mL of TAPN solution of appropriate concentration was added dropwise by pipette. After addition, the solution was allowed to equilibrate for 30 minutes before evaporating the solution in an identical fashion to the other catalysts.

Calcination to decompose the Pt precursor was performed in a tube furnace under 50 sccm flow of dry air (Airgas). All temperature ramps steps were performed at 10˚C/min. 0.4% Pt/SiO_2 was calcined for 300˚C for 2 h, which is above the decomposition temperature of the TAPN precursor in air but minimizes particle sintering and mobility[50]. Likewise, to prepare larger Pt particles, 2% Pt/SiO_2 was calcined at 325˚C for 3 h, and 6% Pt/SiO_2 was calcined at 600˚C for 6 h.

Catalyst Characterization

CO probe molecule diffuse reflectance infrared spectroscopy (CO-DRIFTS) was performed by placing catalyst powder into a Harrick High Temperature reaction cell equipped with ZnSe windows. The prepared cell was then coupled with a Harrick Praying Mantis diffuse reflectance adapter set into a Nicolet iS10 FT-IR spectrometer equipped with a liquid nitrogen-cooled mercury-cadium-telluride (MCT) detector. Prior to characterization, catalysts were pretreated under 50 sccm of 10% H_2/Ar (Airgas) by ramping to 325˚C at a rate of 10˚C/min for 1 h and then cooled to 30˚C under 50 sccm Ar (UHP, Airgas), at which point a background scan was collected. All measurements were performed by averaging 32 scans at a resolution of 0.482 cm^{-1}. After the background scan, 10% CO/Ar (Airgas) was flowed at 50 sccm for 15 minutes to bind CO to the metallic Pt sites. Saturation coverage of CO on the Pt sites was monitored by observing bound CO peak intensity while under CO flow. After 15 minutes of exposure, gas phase CO was purged from the cell by 50 sccm Ar, at which point final spectra were collected showing only CO bound to Pt sites. Spectral deconvolution was performed using 3 Gaussian features, specifically using 2 Gaussians to capture the peak shape of under-coordinated (UC) sites, which typically exhibit an asymmetric shape due to the broad range of geometric and electronic environments (steps, edges, corners, kink, etc.) that these features represent. Site fraction estimates were performed assuming a relative extinction coefficient of 2.7:1 for UC:WC sites, as reported previously[51,52]. Particle size estimates were obtained by relating site fraction estimates to a model cuboctahedron geometry.

CO chemisorption was performed using a Micromeritics Autochem 2920 II chemisorption analyzer. In a typical experiment, 100 mg of catalyst was loaded into the sample U-tube atop quartz wool. Catalysts were pre-treated under 50 sccm of 10% H_2/Ar by ramping from room temperature to 325˚C at 10˚C/min and held for 1 h. After reduction, catalysts were cooled in Ar to 30˚C and purged for an additional 5 minutes. 10% CO/He was introduced from a sample loop of known volume using a 6-way valve at 3.5-minute intervals. The gas atmosphere was analyzed by a thermal conductivity detector (TCD) to measure the amount of CO remaining after exposure to the catalyst sample. Dispersion estimates were made by calculating the CO bound to the Pt catalysts, assuming a $CO:Pt_{surf}$ ratio of 1:1[53].

High-angle annular dark field scanning transmission electron microscopy (HAADF-STEM) images were taken using a Thermo Fisher Talos F200X G2 transmission electron microscope. STEM samples were prepared by adding ground catalysts to methanol (Sigma) and sonicating for 30 minutes, followed by drop casting onto lacey carbon on Cu grids (Ted Pella). The drop cast grids were then kept under vacuum to fully dry for at least 48 hours prior to imaging. Images were collected under an accelerating voltage of 200 kV, and at least 400 particles were imaged to represent the true particle size distributions of the samples.

HDO Reactions

HDO reactions using the prepared catalysts were performed in 75-mL stainless-steel pressure reactors (Parr Instrument Co., 5000 Series). In a typical reaction, 50 mg of catalyst was loaded into the reactor along with 500 mg of dihydroeugenol (DHE, Sigma) and 20 mL of cyclohexane (Sigma). Reactions were stirred magnetically at 700 rpm using glass-shielded stir bars. Once loaded, the reactor was sealed and purged 3 times with 5.0 grade H_2 (Airgas) before pressurizing to a final gauge pressure of 10 bar at room temperature. Then, the vessel was heated to 275 ˚C and held for 2 hours. After the allotted reaction time, the reactor vessel was quickly removed and quenched using a water bath. Once cooled to room temperature, the liquid products were collected by centrifugation and analyzed

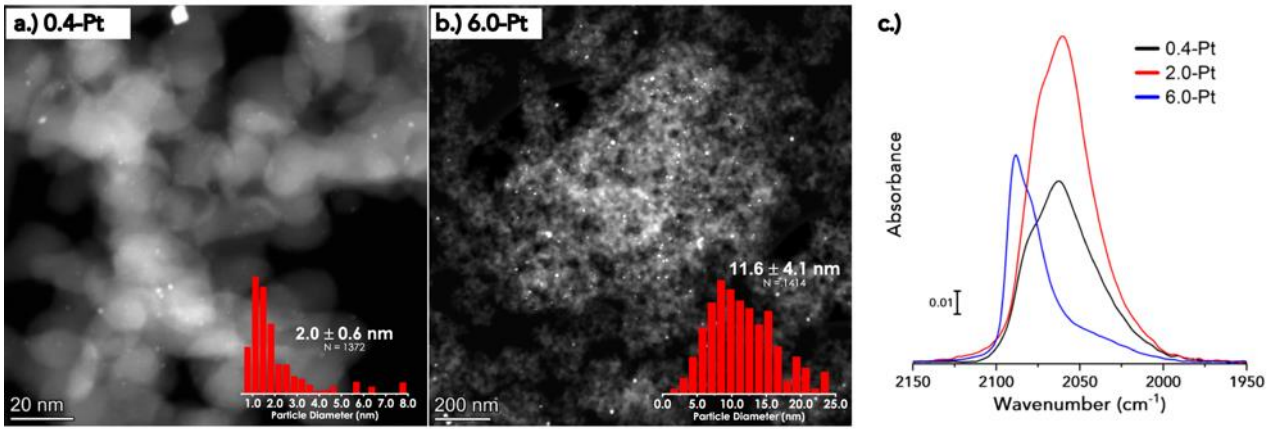

Figure 1: HAADF-STEM images of a.) 0.4-Pt and b.) 6.0-Pt catalysts. Corresponding particle size distributions on a surface area normalized basis are shown as inset images. c.) CO DRIFTS spectra of Pt/SiO_2 catalysts after adsorption of CO at 25˚C following *in-situ* reduction under 10% H_2/Ar at 325˚C for 1 hour.

by GC-FID (Agilent) using n-decane (Sigma) as an internal standard. In some cases, the gas headspace was collected and analyzed by GC. Product identification was carried out using commercially-sourced standards where possible (DHE, 4-propylbenzene, 4-propylphenol, 4-propylcyclohexanol, 4-propylcyclohexane). In instances where standards are not commercially available, FID responses were estimated using effective carbon number (ECN)[54–56]. Reaction performance

$$Conversion\ (\%) = \frac{N_{DHE}^{\square}}{N_{DHE}^{0}}$$

$$Selectivity\ (\%) = \frac{N_{Product}}{\sum N_{Product}^{\square}}$$

$$Yield\ (\%) = \frac{N_{Product}}{\sum N_{Product}^{\square}} * Conversion$$

metrics were defined as:

where N_i is the number of moles of species i measured by GC-FID and N_i^0 is to the initial number of moles of i loaded into the batch reactor. For isoconversion experiments, conversion of substrate was altered by changing the catalyst loading into the reactor, thus moderating the catalyst:substrate mass ratio.

Results

Catalyst Characterization

To elucidate the sensitivity of phenolic HDO chemistry to the structure of active sites on metal nanoparticle surfaces, catalysts containing varying distributions of Pt particle sizes were synthesized on high surface area SiO_2 supports (170+ m^2/g) by altering Pt weight loading and calcination treatment conditions. Focus was placed on varying Pt particle sizes between an average of 1 and 10 nm in diameter, as the fraction of under-coordinated sites (steps, edges, etc.) and well-coordinated sites (planar terraces such as (111) and (100) planes) exposed on metal nanoparticle surfaces change most significantly in this size range (Figure S1). SiO_2 was chosen as the support because of its inactivity in HDO[57,58], which isolates the influence of Pt size and active site structure on HDO chemistry. However, the synthesis of late transition metal catalysts with controlled metal particle size distributions on SiO_2 is a known challenge. Both metal precursors and the metallic particles themselves bind weakly to the SiO_2 surface[59,60], resulting in aggregation and sintering upon elevated thermal treatment, such as those found during calcination, reduction, or HDO reactions[48,61]. This behavior has led researchers to deem the SiO_2 surface an "ice skating rink"[62], aptly capturing the difficulty of immobilizing supported materials on these surfaces, which can result in catalyst samples with broad distribution of particle sizes.

Pt/SiO_2 catalysts were prepared using strong electrostatic adsorption[48,49] (SEA) with metal loadings ranging from 0.4 wt% to 6 wt%. These materials were then treated by different calcination conditions (0.4 wt% at 300 ˚C, 2 wt% at 325 ˚C, and 6 wt% at 600 ˚C) to produce catalysts with distinct Pt nanoparticle distributions, summarized in Table 1. The catalysts are named X-Pt, where X indicates the catalyst weight loading (i.e. 0.4-Pt for 0.4 wt% Pt). The catalysts were characterized by HAADF-STEM, CO DRIFTS, and CO chemisorption. Each technique provides a different estimate for average Pt particle size depending on the size distribution, particle shape, and sample pretreatment[63–65].

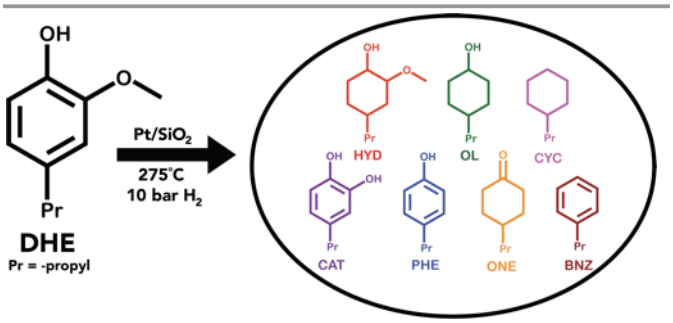

Scheme 2 Structures and naming convention used in discussion for DHE and its products identified by GC-FID. Products (*left to right*): 4-propyl-2-methoxycyclohexanol (HYD), 4-propylcyclohexanol (OL), 4-propylcyclohexane (CYC), 4-propylcatechol (CAT), 4-propylphenol (PHE), 4-propylcyclohexanone (ONE), 4-propylbenzene (BNZ).

Table 1

Sample	Calcination Treatment	Mean Particle Size (nm)				
		TEM			CO DRIFTS[d]	CO Chemisorption[e]
		Counts[a]	S.A. Normalized[b]	Volume Normalized[c]		
0.4-Pt	300˚C, 2 hours	1.3 ± 0.6	2.0 ± 0.6	3.1 ± 0.6	<1.1	3.8 ± 0.3
2.0-Pt	325˚C, 3 hours	1.4 ± 0.9	3.0 ± 0.9	4.6 ± 0.9	1.6	4.9 ± 1.2
6.0-Pt	600˚C, 6 hours	6.8 ± 4.1	11.6 ± 4.1	13.8 ± 4.1	2.9-7.1	44 ± 17

Overview of catalyst preparation conditions and average Pt particle size determined by various complementary methods.[a] Average particle diameter by hemispherical area.[b] Average particle diameter normalized as $\sum d_i^3/d_i^2$.[c] Average particle diameter normalized as $\sum d_i^4/d_i^3$.[d] Estimated from deconvolution of linearly bound CO on Pt feature in Figure 1 DRIFTS spectrum.[e] Estimated from $\langle d \rangle = 1.01/D$, where D is the measured dispersion assuming a [CO]/[Pt] ratio of 1.

Volumetric CO chemisorption following *in situ* H_2 reduction showed Pt dispersions ranging from 26% for 0.4-Pt to 2% for 6.0-Pt. Based on assumptions of hemispherical particles[66], average Pt particle sizes were estimated to be 3.8 nm (0.4-Pt) to 44 nm (6.0-Pt), as shown in Table 1. The estimated average Pt particle size increases with Pt loading and calcination temperature, consistent with particle aggregation caused by greater Pt surface density and sintering.

To provide more insight into the Pt particle size distributions, HAADF-STEM images were collected. Particle size averages and distributions are presented using counts, surface-area-normalization, and volume-normalization. These three data presentations result in distinct averages and distributions due to changing surface area:volume ratio as a function of particle size, which is demonstrated in Figure S5. Typical images of the 0.4-Pt and 6.0-Pt catalysts are shown in Figures 1a and 1b, along with the surface area-normalized particle size distributions. Additional STEM images, including those for 2.0-Pt, are shown in Figures S2-4. The surface area-normalized average particle sizes and distributions are used since nanoparticle surface properties directly influence the reactivity of heterogeneous catalysts. The average Pt particle size increases with Pt weight loading, from 2.0 ± 0.6 nm for 0.4-Pt to 3.0 ± 0.9 nm for 2.0-Pt, and to 11.6 ± 4.6 nm for 6.0-Pt, highlighting a consistent trend with the CO chemisorption results.

As shown in Table 1, STEM-based particle size estimates are lower than chemisorption-based values. This is attributed to outliers in the particle size distributions. Using 0.4-Pt as an example, particle size distributions from HAADF-STEM images show that although there are only 22 out of 1372 (~2%) counted particles greater than 3 nm in size, these outlier particles contain ~40% of the total imaged Pt volume (Figure S6). These outlier particles contribute to the measured CO chemisorption values (a volume-normalized analysis), but less so to surface area-normalized analysis (e.g. reactivity and surface area normalized TEM). This can be seen in the better agreement in average particle sizes obtained via CO chemisorption and volume-normalized STEM images.

HAADF-STEM and chemisorption measurements were complemented by CO DRIFTS, which benefits from being a sample-averaged, bulk measurement, similar to CO chemisorption, yet provides particle size estimates based on only metal surface properties, analogous to surface-normalized HAADF-STEM. The vibrational frequency of CO adsorbed on Pt is sensitive to the Pt coordination number, allowing for identification of CO adsorbed to well-coordinated (WC, 8+ coordinate) Pt sites, located at the surface of flat, low-index terraces, and under-coordinated (UC, 7 or fewer coordinate) sites, which are found at steps, edges, corners, and other structural defect sites[67,68]. The ratio of these sites on Pt surfaces is known to be a function of particle size[69–71].

Figure 1c shows CO DRIFTS spectra at saturation CO coverage and room temperature for the Pt catalysts following in situ reduction in H_2. Each spectrum consists of a complex feature centered between 2097 and 2050 cm^{-1}, consistent with the C-O stretching frequency of CO bound linearly atop Pt atoms with varying coordination numbers[69–73]. The change in position of the observed CO stretching frequency stems from both the convolution of the individual features associated with CO adsorbed to WC and UC Pt sites at ~2090-2080 and ~2070-2050 cm^{-1}, respectively[65,67], as well as shifts related to CO dipole-dipole interactions[74–76]. Deconvolution of the CO DRIFTS spectra using 3 Gaussian features, as described in more detail in Figure S7, results in estimated average particle sizes of ~1 nm to 7 nm for the 0.4-Pt and 6.0-Pt catalysts, respectively. Overall, CO DRIFTS estimates follow the same trend in average particle size as observed from both HAADF-STEM and CO chemisorption measurements. CO DRIFTS provided the smallest average Pt particle size estimate from the three techniques, likely due to CO-induced roughening of Pt surfaces, which causes an over-estimation of the UC relative site concentration[65]. Despite small discrepancies, the particle size estimates from CO-DRIFTS are in better agreement to surface-normalized HAADF-STEM distributions than estimates from CO chemisorption, suggesting that the CO DRIFTS analysis is less skewed by the presence of outlier particles in broad particle size distributions. Regardless of technique used, the results consistently demonstrate that the Pt/SiO_2 catalysts prepared exhibit distinct average particle size distributions and provide sufficient variation of surface composition to determine the structure sensitivity of HDO.

HDO Reactions

Table 2

Sample	Catalyst Loaded (mg)	Conversion (%)	Rate ($\frac{mmol_{DHE}}{hr*g_{Pt}}$)	TOF (hr^{-1})
0.4-Pt	50	14	1053	790
2.0-Pt	15	15	752	712
6.0-Pt	20	8	100	848

Catalyst amount, observed DHE conversion, DHE consumption rate and TOF for Pt/SiO_2 catalyst series in the HDO of DHE. *Conditions:* 275˚C, 2 hours, 20 mL cyclohexane, 500 mg DHE, 10 bar H_2.

The Pt/SiO_2 materials described above were used to catalyze HDO of the multi-oxygenated lignin model compound dihydroeugenol (DHE). Liquid-phase batch reactions were conducted in a high-pressure reactor at 275˚C using cyclohexane as a solvent. To ensure comparability between Pt/SiO_2 catalysts, reactions were initially conducted at isoconversion, moderated by changing catalyst loading into the reactor, and reaction performance was analyzed by quantifying DHE conversion and product yield using GC-FID. The analysis of reactions at isoconversion is essential for complex reaction networks in which substrate conversion and product selectivity are intrinsically linked[77-79]. The investigation of low DHE conversions (<15%) and short reaction times (under 2 hours) ensured that the studies of HDO structure sensitivity were made in the absence of catalyst deactivation effects (vide infra), which is a known challenge for HDO of oxygenates[80-82]. For all Pt/SiO_2 catalysts studied, product analysis of the liquid phase resulted in the quantification of 7 major products, shown in Scheme 2, which include both partially and fully deoxygenated species. Mass balances calculated on the basis of C_6 ring products for the isoconversion experiments in Table 2 and Figure 2 were above 87% for all catalysts, indicating that the products shown here capture the primary reactivity. The remaining mass not quantified by GC-FID is attributed to the formation of strongly bound adsorbates (Table S5) and oligomers which cannot be measured by GC-FID and are

ubiquitously observed under comparable reaction conditions[83-86]. Analysis of the gas phase products in the head space of the reactor (Figure S10) indicates the formation of CH_4, CO, and methanol likely stemming from demethoxylation and demethylation, with no evidence of light hydrocarbons stemming from cracking reactions. Thus, gaseous products do not need to be accounted for in the mass balance.

Table 2 shows rates of DHE consumption estimated using the measured conversion at 2 hours, normalized by the amount of Pt loaded into the reactor. A DHE conversion of 14% was observed after 2 hours under reaction conditions for 50 mg of 0.4-Pt, while 20 mg of the 6.0-Pt catalyst reached 8% DHE conversion in a 2-hour reaction. The DHE consumption rates calculated on a Pt weight basis are 10-fold higher for 0.4-Pt as compared to 6.0-Pt. However, after normalizing the DHE consumption rates by the active Pt site density measured by CO chemisorption, the turnover frequencies (TOF) for DHE are comparable for all 3 catalysts. It is important to note that due to the complexity of the reaction network, these estimates do not capture differences in estimated rates for individual reactions, such as hydrogenation and deoxygenation, but rather capture the similar per site rates of DHE consumption. Still, the comparable TOF's across the three catalysts are indicative of a shared rate-limiting step prior to the structure-sensitive steps discussed below. One explanation may be saturation of the Pt surface by adsorbates, causing adsorption to be kinetically-relevant for all catalysts, while product selectivity is dictated by the subsequent reaction steps. Another possibility is that structure-insensitive deactivation through site blocking by oligomeric species is occurring, leading to inaccurate TOF estimations due to transient changes in site availability.

Analysis of the product selectivity (Figure 2) reveals that there are differences in the observed products with variation in Pt particle size distribution. The most apparent trend is the significant drop in 4-propylphenol (PHE) selectivity with

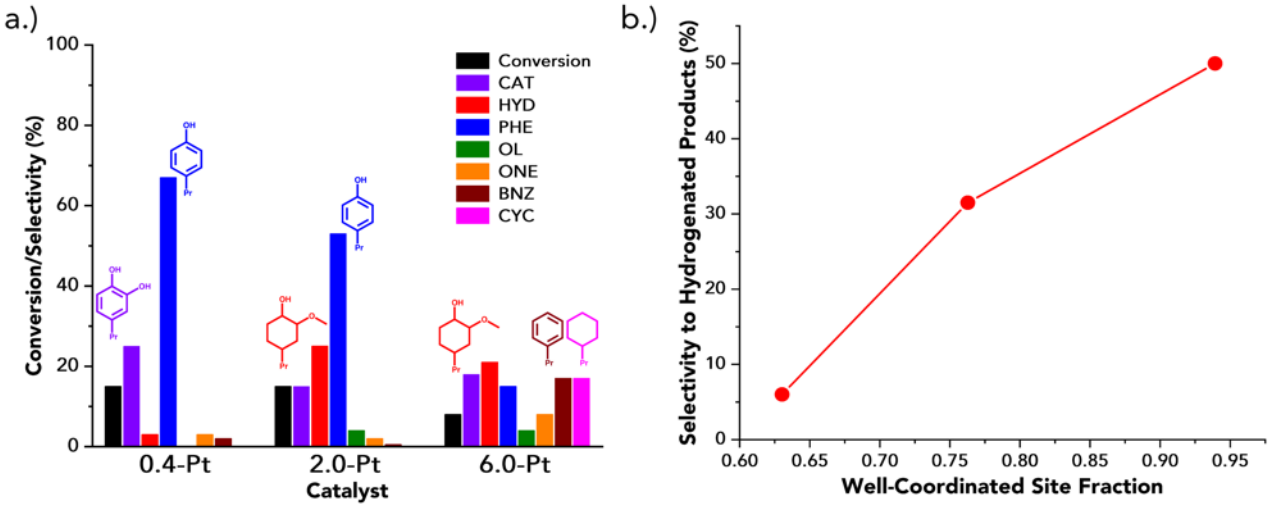

Figure 2 Results of DHE HDO reactions at isoconversion (~15%) over various-sized Pt catalysts. a.) Selectivity breakdown of all species detected by GC-FID for DHE HDO. b.) Grouping of hydrogenated products (HYD, OL, ONE, CYC) from DHE HDO shows clear trend with increasing particle size. Conditions: 500 mg DHE, 275˚C, 2 hours, 20 mL cyclohexane, 10 bar H2

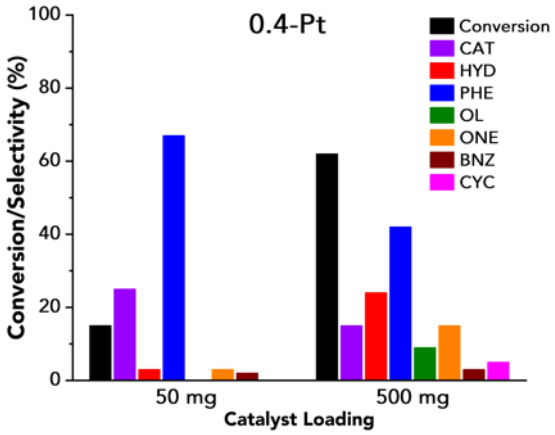

Figure 3 HDO reactions of DHE investigating the influence of 0.4-Pt catalyst loading on product selectivity. Results demonstrate that the selective formation of PHE by 0.4-Pt persists at significantly higher conversions than shown in Figure 2, underscoring that this behavior stems from the structure sensitivity of HDO over Pt/SiO2 catalysts. Conditions: 500 mg DHE, 275˚C, 2 hours, 20 mL cyclohexane, 10 bar H2.

increasing average Pt particle size. PHE is presumably the product of direct demethoxylation of DHE (partial HDO), though this will be discussed later. PHE is the primary product over 0.4-Pt at 68% selectivity, as well as over 2.0-Pt, albeit at a lower selectivity of 53% due to increasing selectivity to off-target products such as 4-propyl-2-methoxycyclohexanol (HYD), the product of DHE ring hydrogenation. This trend continues with 6.0-Pt, which exhibits the lowest selectivity to PHE after 2 hours of reaction at 15%. It is worth noting that there is no evidence of initial attack on the hydroxyl group of DHE to yield anisole derivatives or the HDO products of anisole derivatives. Initial deoxygenation occurs through the methoxy functionality of DHE, consistent with the weaker bond strength of the C-OCH_3 bond[33].

In addition to PHE formation, the production of 4-propylcatechol (CAT) via DHE demethylation is also observed. CAT is the only other major product formed by 0.4-Pt, with a selectivity of 25%. However, unlike the monotonic trend observed for PHE formation with increasing Pt particle size across the catalyst series, there is no discernible trend of CAT selectivity as a function of particle size distribution. 2.0-Pt and 6.0-Pt have CAT selectivities of 15% and 18%, respectively, similar to what was observed for 0.4-Pt despite the marked differences in PHE productivity, Pt loading, and average Pt particle size.

Another clear trend exists between average Pt particle size and selectivity to the hydrogenated products (4-propyl-2-methoxycyclohexanol, HYD; 4-propylcyclohexanol, OL; 4-propylcyclohexanone, ONE; 4-propycyclohexane, CYC), which are the result of ring hydrogenation of DHE, PHE, or 4-propylbenzene (BNZ), respectively. The production of these species is summarized in Figure 2b, showing the collective selectivity towards these 4 products as a function of well-coordinated (WC) Pt site fraction, estimated from average particle size using the cuboctahedron model geometry[65,87]. As discussed above, 0.4-Pt demonstrates negligible formation of these products, indicating a low rate of aromatic ring hydrogenation despite the occurrence of partial HDO of DHE to PHE and CAT. Activity towards aromatic hydrogenation increases with increasing Pt particle size, with 2.0-Pt producing 32% hydrogenated ring products and 6.0-Pt increasing to 50%. For 2.0-Pt, the increase is primarily driven by an increased selectivity to HYD, which constitutes 23% of the overall products, although PHE remains the dominant product. HYD selectivity does not increase in the case of 6.0-Pt, and instead the increase to total hydrogenated products is driven primarily by increased selectivity to CYC at 17%. In contrast, 0.4-Pt and 2.0-Pt did not produce detectable quantities of CYC.

The increased activity of 6.0-Pt to CYC production is accompanied by an increased production of BNZ at 17% selectivity of the overall products. Thus, 6.0-Pt provides the highest activity for complete HDO to fully-deoxygenated products, in addition to exhibiting the highest rates of ring hydrogenation. It is worth noting the nearly equal selectivity of BNZ and CYC in the case of 6.0-Pt, despite the observed ability of 6.0-Pt to effectively perform aromatic ring hydrogenation. This is analogous to the results of 0.4-Pt and 2.0-Pt reactions, where BNZ is observed in small quantities (<2% selectivity), but CYC is not observed. Additionally, the production of BNZ and CYC is expected to be unrelated to the hydrogenation activity of 6.0-Pt, as previous work has shown Pt/SiO_2 catalysts do not facilitate the HDO of saturated oxygenates[58].

Deactivation due to strong adsorption of substrates and intermediates is a known issue for HDO catalysts, particularly for small nanoparticles and clusters exhibiting a large fraction of UC sites which bind oxygenates more strongly than WC sites[44]. To ensure that differences in the isoconversion experiments were not a result of deactivation of Pt/SiO_2 catalysts, HDO of DHE over 0.4-Pt was carried out in the presence of 500 mg catalyst to reach a higher DHE conversion of 62%, as shown in Figure 3. Exhibiting the smallest average particle size and thus the highest fraction of UC sites, the 0.4-Pt catalyst is expected to be most affected by deactivation. However, Figure 3 shows

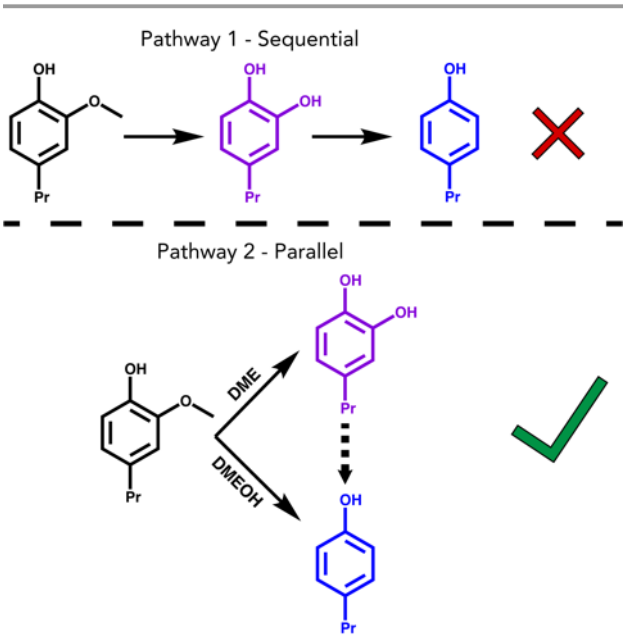

Scheme 3 Proposed pathways for initial deoxygenation of DHE via either sequential or parallel schemes. Time profile reactions evidence the parallel formation of CAT and PHE via independent routes (Pathway 2)

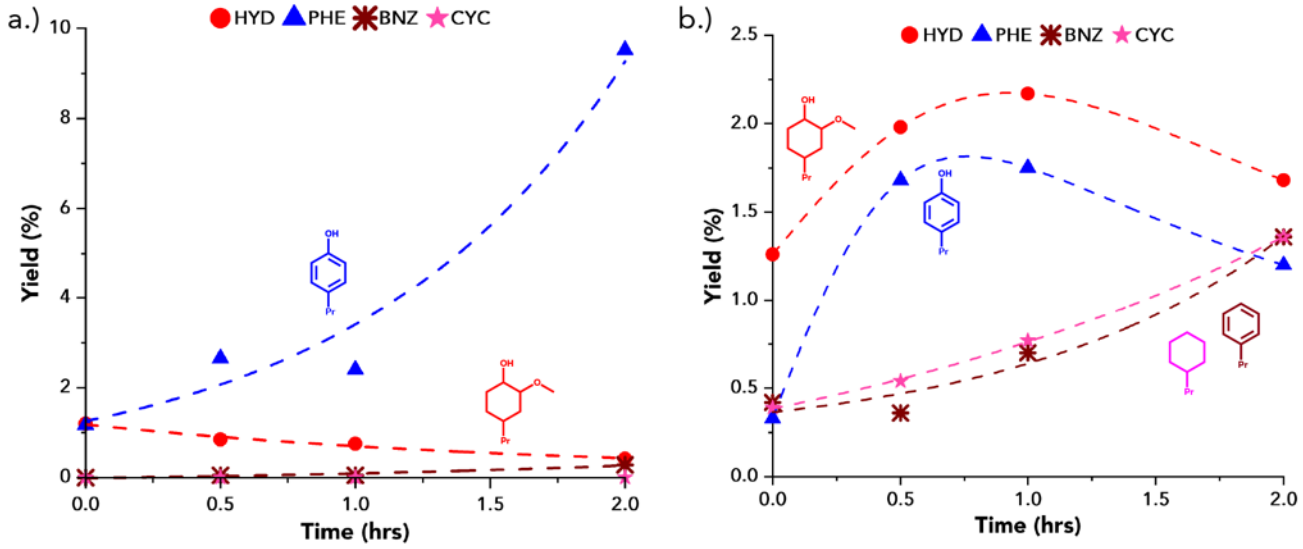

Figure 4 Selected product yield as a function of reaction time for a.) 0.4-Pt and b.) 6.0-Pt. Lines are included to guide the eye only and do not represent kinetic fits. Product distributions are expressed in yield rather than selectivity to clarify changes in time due to changing conversion as well as selectivity. Black circles (**o**) and the corresponding black dotted line (- - -) represent conversion levels with time. *Conditions*: 500 mg DHE, 50 mg cat., 275˚C, 10 bar H_2, 20 mL cyclohexane. Complete time profiles for all species can be found in the Supplementary Information (Figure S12).

that the product selectivity trends are comparable at both 15% and 62% conversion of DHE. PHE remains the dominant product at 42% of the products, indicating that the 0.4-Pt catalyst is effective for DHE demethoxylation over hydrogenation even at high conversions. In the high conversion experiment, HYD, OL, and ONE selectivities are all higher than in the isoconversion experiment but remain minor products relative to PHE. This contrasts experiments performed over 6.0-Pt, over which HYD was the dominant product. Therefore, the structure sensitivity observed in the isoconversion experiments is not a result of catalyst deactivation, but rather differences in the intrinsic reactivity of DHE over different Pt sites.

The isoconversion results demonstrate that the product distribution of DHE HDO is sensitive to the average particle size of Pt/SiO_2 catalysts and thus the geometry of the exposed active Pt sites. However, single time-point experiments alone cannot determine the reaction pathways by which final products are formed, which contain vital information as to the specific reactions exhibiting structure sensitivity. For example, it is unclear whether PHE is produced directly from DHE via demethoxylation or if PHE is formed from CAT via dehydroxylation, as shown in Scheme 2. To explore this and identify the transience of product formation in DHE HDO, time profile experiments were conducted between 0 and 2 hours at 275˚C under 10 bar of H_2, shown in Figure 4. Focus was placed on the 0.4-Pt and 6.0-Pt catalysts, as these exhibited the greatest differences in product selectivity in the isoconversion experiments. Catalyst loadings were identical to those described in Table 2.

A notable feature of the batch reactor set-up is the introduction of catalyst and substrate to the reactor at room temperature, resulting in measurable activity during the thermal ramping stage to reaction temperature. To account for this, the data profile for 0 hours represents reactions that were set up and allowed to ramp to 275˚C before immediately quenching the reaction. Figure 4a shows the time profile experiments for 0.4-Pt, which exhibits the aforementioned reactivity during the thermal ramp, resulting in 1.5% conversion at 0 hours. Interestingly, it can be seen that a major reaction during the thermal ramp is aromatic ring hydrogenation of DHE to form HYD, which was only a minor product over 0.4-Pt during 2-hour reactions at 275˚C. This is consistent with the lower apparent activation barriers reported for aromatic ring hydrogenation over Pt catalysts (50-100 kJ/mol[88]) compared to apparent barriers for HDO (100-200 kJ/mol[28,89-90]); thus, at temperatures below 275˚C, hydrogenation is facilitated relative to HDO over 0.4-Pt.

At 275˚C, DHE conversion increases from 3% at 0 hours to 14% at 2 hours. During this period, PHE and CAT are produced and become the dominant products, as seen in the isoconversion experiments. At the same time, overall HYD yield falls, indicating HYD consumption in the reaction. Considering the inability of Pt/SiO_2 catalysts to perform deoxygenation on saturated species[58], we attribute this consumption to dehydrogenation to reform the original DHE substrate, which can then undergo deoxygenation at reaction temperatures to form PHE and CAT. This points to an interesting role of hydrogenation and dehydrogenation over 0.4-Pt which will later be discussed. As noted in the isoconversion experiments, production of other deoxygenated species such as OL, ONE, BNZ, and CYC is minimal over 0.4-Pt (Figure S12). One notable trend is the monotonic loss of OL yield paired with increasing ONE and BNZ yields. The greatest OL yield occurring during the thermal ramp is consistent with the hydrogenation activity of 0.4-Pt below reaction temperature, as seen in the behavior of HYD formation.

The production of PHE and CAT occurs at similar rates over the reaction period, increasing in yield from their original values of 1.2% and 0.4%, respectively, to 9.5% and 3.5%, corresponding to final selectivities of 54% and 35%. However, what is not observed is the increase of PHE yield at the expense of CAT yield, which is what would be expected in a sequential reaction scheme (Scheme 3). Instead, the simultaneous formation of PHE and CAT supports parallel formation of both

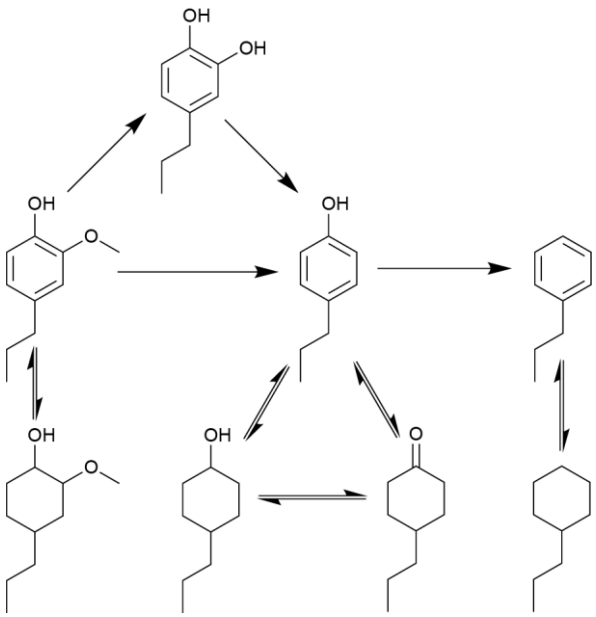

Scheme 4 Overall proposed scheme of DHE HDO over Pt/SiO_2. Single arrows represent steps which are observed to be irreversible under the reaction conditions studied. Double arrows indicate reactions which show evidence of being reversible, though not necessarily at equilibrium or quasi-equilibrated.

products through distinct pathways of demethylation and demethoxylation of DHE. Though interconversion of CAT and PHE cannot be entirely excluded, it is apparently not the dominant pathway of PHE formation under the conditions studied here. This also suggests that the structure sensitive reaction in the formation of PHE from DHE is indeed demethoxylation, and not the conversion of CAT to PHE. Similarly, the demethylation of DHE to CAT is not apparently structure sensitive, as evidenced by the nearly constant selectivity to CAT across all Pt/SiO_2 catalysts studied.

Time profile experiments over 6.0-Pt (Figure 4b) show different trends. As with 0.4-Pt, HYD formation is dominant during the thermal ramp. However, unlike 0.4-Pt, HYD yield continues to increase up to 1 hour before decreasing slightly at 2 hours. This contrasts with 0.4-Pt reactions, where HYD concentration decreases monotonically during the time profile experiments due to dehydrogenation to DHE. This is consistent with the reported structure sensitivity of dehydrogenation[92], which has pointed towards smaller nanoparticles being more effective catalysts for dehydrogenation. Thus, the larger nanoparticles present in the 6.0-Pt catalyst perform dehydrogenation less effectively than 0.4-Pt, but more effectively catalyze hydrogenation of DHE to HYD.

The most striking difference in 6.0-Pt performance over the 2-hour time profile compared to 0.4-Pt reactions is the production and consumption of PHE. PHE yield rises from 0.3% to 1.8% over 1 hour, before falling to 1.2% at 2 hours. Concomitant with the consumption of PHE between 1 and 2 hours is the rise of BNZ and CYC yields to 1.4% each at the end of the 2-hour reaction period. Clearly, PHE is an intermediate to form CYC and BNZ, but this pathway was not facilitated over 0.4-Pt. CAT formation over 6.0-Pt follows a similar trend as was observed over 0.4-Pt, and additionally does not undergo any obvious consumption during the reaction period. It follows that CAT is not an intermediate towards the formation of CYC and BNZ, which apparently form only from PHE.

The time profiles highlight two trends that were not apparent in the isoconversion experiments (Figure 2). First, 0.4-Pt performs dehydrogenation at reaction temperature, as shown in the loss of HYD yield with time, resulting in higher yields of aromatic products. On the other hand, 6.0-Pt does not facilitate facile dehydrogenation, thus leading towards off-target hydrogenated products such as HYD. Second is the greater ability of 6.0-Pt to form deeper deoxygenated products such as BNZ and CYC from DHE, specifically through the conversion of PHE. This supports the conclusions from the isoconversion experiments over 6.0-Pt, and contrasts the inability of 0.4-Pt to facilitate the HDO of PHE. Clearly, deoxygenation of PHE is distinct between the 0.4-Pt and 6.0-Pt catalysts and causes the discrepancy in fully-deoxygenated BNZ and CYC formation (Scheme 4).

As evidenced from the time profiles, although 0.4-Pt catalyzes dehydrogenation of HYD back to DHE prior to HDO to deoxygenated species, hydrogenation to HYD clearly occurs during the thermal ramp. Since both reactions appear to be kinetically accessible over this catalyst, what was not immediately clear was the high yield of PHE over 0.4-Pt over a range of conversions (Figure 3) and time (Figure 4a) without significant hydrogenation of PHE to OL and ONE. One potential explanation of this is the ability of 0.4-Pt, through facile hydrogenation and dehydrogenation, to approach the equilibrium composition of saturated and unsaturated products. To explore this further, the HDO of DHE was studied over 0.4-Pt with varying initial H_2 pressures between 5 and 20 bar. A higher isoconversion level of 50% was targeted for each pressure, in comparison to the 10% isoconversion studied initially in Figure 2, to allow comparison of the product distribution at an advanced state in the reaction network after multiple potential reactions such as deoxygenation and hydrogenation.

Figure 5 shows that reactions over 0.4-Pt at 5 bar initial H_2 result in high selectivity to PHE of 66%, even at 54% conversion of DHE, which is almost identical to the PHE selectivity seen in Figure 2 at ~15% DHE conversion. Increasing H_2 pressure to 10

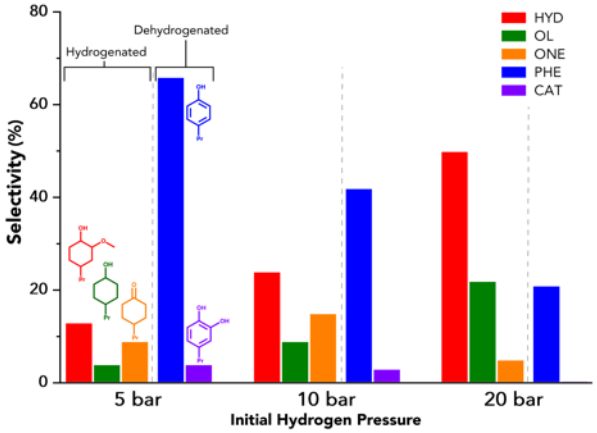

Figure 5: HDO reactions of DHE conducted under varying initial H_2 pressure using the 0.4-Pt catalyst. Conducted at isoconversion of ~50% by adjusting catalyst loading. *Conditions*: 500 mg DHE, 275˚C, 2 hours, 20 mL cyclohexane

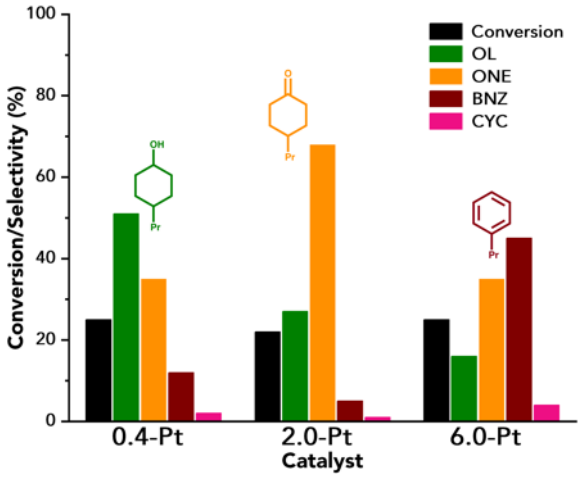

Figure 6 HDO reactions at isoconversion of PHE over various sized Pt catalysts. *Conditions*: 500 mg DHE, 275˚C, 2 hours, 10 bar H_2, 20 mL cyclohexane. Catalyst loading was varied to achieve isoconversion of 25% across all catalysts.

bar results in an increase of HYD selectivity to 24% at the expense of PHE, which drops to 42%, as well as an increase in OL and ONE selectivities to 9% and 15% respectively, though PHE remains the dominant product. Further increasing pressure to 20 bar results in a continuation of this trend, with HYD becoming the dominant product at 50% selectivity, with OL and PHE selectivities becoming approximately equal at 21% and 22%. These results show that the extent of hydrogenation over 0.4-Pt is not inhibited by the catalyst structure, but rather is dictated by the pressure of H_2.

Also, HYD selectivity increases to a greater extent with increasing H_2 pressure than OL and ONE selectivity. The increase in HYD selectivity represents decreasing HDO activity, as HYD is not the product of any deoxygenation. This supports the observation that non-acidic catalysts such as Pt/SiO_2 studied here are not active for conversion of saturated species such as HYD, which act as dead end in the HDO pathway unless they are able to undergo dehydrogenation back to aromatic species. This is also supported by pressure dependent studies carried out over 6.0-Pt (Figure S11), which showed decreasing BNZ and CYC yield with H_2 pressure with increasing HYD yield. Thus, increasing H_2 pressure decreases yield for Pt/SiO_2 catalysts by facilitating dead-end product formation.

To understand the mechanistic differences between 0.4-Pt and 6.0-Pt in PHE dehydroxylation, HDO reactions starting from PHE as the substrate were conducted at 275˚C for 2 hours under 10 bar H_2, shown in Figure 6. Isoconversion conditions were achieved at approximately 25% conversion, moderated by different catalyst loading for each reaction. The product distributions demonstrate that there are again differences caused by Pt particle size distribution. Consistent with the observations of reactions using DHE as a substrate, 0.4-Pt and 2.0-Pt both catalyze relatively little conversion to BNZ and CYC, despite starting from PHE, a less oxygenated substrate than DHE. This is also consistent with the time profile results of 0.4-Pt, wherein PHE was effectively produced from DHE, but did not appreciably react further. There is also a shift in the dominant product from OL to ONE in PHE HDO between 0.4-Pt and 2.0-Pt, respectively, suggesting that there is some difference in the hydrogenation chemoselectivity of these two catalysts.

PHE HDO results over 6.0-Pt are consistent with prior reactions starting from DHE, as 6.0-Pt is highly active to the formation of BNZ, demonstrating once again the ability of 6.0-Pt to facilitate complete deoxygenation. Interestingly for the HDO of PHE in Figure 6, BNZ selectivity is greater than CYC at 45% for BNZ compared to 4% for CYC, perhaps due to the greater conversions reached in these experiments compared to the isoconversion experiments previously at ~10%. Once again, this can be explained by a reaction pathway wherein BNZ forms directly from PHE, and only then undergoes subsequent hydrogenation of BNZ to form CYC. Overall, these results demonstrate that the 6.0-Pt catalyst is uniquely capable of facilitating HDO of both mono- and multi-oxygenated phenolics.

Discussion

The results shown above demonstrate a clear effect of Pt nanoparticle size distribution (and thus exposed Pt site structure) on activity and selectivity in the HDO of multifunctional oxygenated substrates, highlighting that these trends have broad effects for HDO of aromatic phenols derived from lignin outside of model systems. However, it is important to consider how the Pt particle size effect is manifested in these complex networks, as numerous steps in the HDO reaction scheme may be individually responsible for the observed behavior. In order to concisely interpret these results in the context of the HDO reaction network, we summarize our findings as follows:

1. Hydrogenation of the aromatic ring in lignin model phenolics is structure sensitive over Pt/SiO_2 catalysts. Catalysts with larger Pt particle sizes increase the selectivity to hydrogenated products (HYD, OL, ONE, CYC), thus indicating that well-coordinated sites on low-index planes of metal nanoparticles are responsible for planar aromatic adsorption, which facilitates aromatic hydrogenation.
2. Demethoxylation also exhibits structure sensitivity, with increased selectivity to demethoxylated products over smaller Pt particle sizes. In contrast to ring hydrogenation, under-coordinated sites of Pt nanoparticles at steps, edges, and other defects are active indicating that planar adsorption is not necessary for demethoxylation.
3. Hydrogenated and dehydrogenated products exist in an equilibrium in the liquid phase batch reactions and are dictated in part by the H_2 pressure.
4. Dehydroxylation, HDO of phenolic hydroxyl group, is structure sensitive over Pt/SiO_2 catalysts. Surprisingly, and in contrast to suggestions made previously in the literature[43-45], increased selectivity to fully deoxygenated hydrocarbons is observed for larger Pt particle sizes, suggesting that WC sites on Pt terraces are the active site for dehydroxylation of phenolics under the conditions studied here.

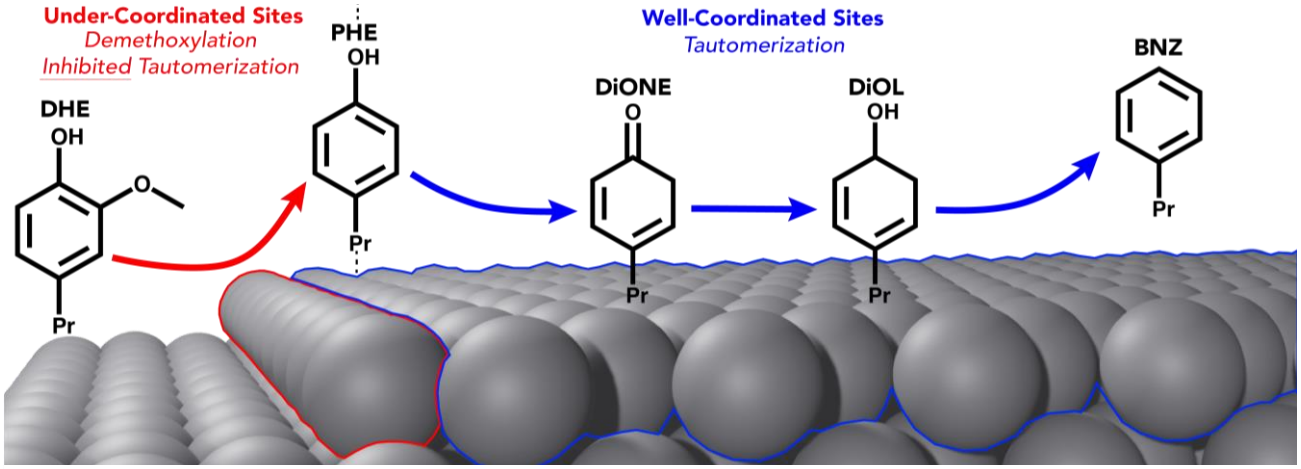

Scheme 5 Summary of the structure sensitivity of deoxygenation steps in the HDO of DHE over Pt/SiO_2 catalysts. PHE deoxygenation proceeds through tautomerization over WC sites, explaining the observed production of BNZ and CYC over 6.0-Pt but not 0.4-Pt. Aromatic ring hydrogenation and dehydrogenation reactions, which also exhibit structure sensitivity, have been omitted from this scheme since these do not contribute directly towards deoxygenation.

The contextualization of these results lends further insight into the fundamental nature of structure sensitivity over Pt/SiO_2 catalysts shown here. Considering first the structure sensitivity of aromatic ring hydrogenation, we identify through increased selectivity to hydrogenated products that WC sites present on low-index, planar Pt terraces are the active site for ring hydrogenation. This observation is consistent with findings from previous literature on hydrogenation of aromatic hydrocarbons such as benzene[41,92]. Phenolic ring hydrogenation pathways over Pt require planar adsorption of the substrate to the Pt surface, which leads to disruption of ring aromaticity and facilitates hydrogenation. Importantly, planar aromatic adsorption is not facilitated by stepped surfaces or over edges, as the ring requires a contiguous planar surface upon which to adsorb to maximize substrate-metal interaction[93].

Demethoxylation, on the other hand, is apparently less geometrically demanding and is facilitated over small nanoparticles with UC sites located at steps, edges, and other defect sites. Hence, demethoxylation does not require planar adsorption of the aromatic ring. Non-planar adsorption modes have previously been identified by spectroscopy on the surface of metal catalysts[94] and have been attributed to facilitate C-O cleavage as a result of specific interaction of the metal surface with the C_{Aryl}-OCH_3 bond. The occurrence of demethoxylation over UC sites is also consistent with the greater binding strength of methoxy fragments and methanol to these sites, in turn creating a thermodynamic driving force for the reaction over these sites[95]. Our results also suggest that demethylation of DHE to CAT is a parallel reaction competing with demethoxylation, and not a sequential pathway from DHE to CAT to PHE. Interestingly, the demethylation of DHE to form CAT is not structure sensitive over the Pt/SiO_2 catalysts studied here, resulting in similar selectivity of CAT across all catalysts.

Our results also highlight the influence of hydrogen pressure on product selectivity. At high conversions (60%), selectivity of the 0.4-Pt catalyst favored the aromatic compounds PHE and CAT over saturated hydrocarbon products for pressures at or below 10 bar of H_2. Importantly, the reactor contains at least 4.6 molar equivalents of H_2 relative to DHE when pressurized to 5 bar, indicating that for all reactions aromatic hydrogenation is not stoichiometrically limited. At 20 bar H_2, the saturated products HYD and OL became dominant. These results demonstrate that 0.4-Pt exhibits the sites necessary for hydrogenation, though these sites are scarce relative to 6.0-Pt as shown by the lower extents of ring hydrogenation during the thermal ramp over 0.4-Pt compared to 6.0-Pt. Therefore, the production of aromatic products over 0.4-Pt is not a result of a structurally-limited capacity for ring hydrogenation. Instead, the kinetic accessibility of dehydrogenation over UC sites present on the 0.4-Pt catalyst enables the system to approach an equilibrium determined by the H_2 pressure. To support this, equilibrium calculations were made for phenol hydrogenation as a simplified model system. These calculations suggest that despite the stoichiometric excess of H_2 present at all pressures studied, equilibrium positions at 275˚C favors the formation of aromatic products such as phenol (S.I. Note 1). Comparatively, over the 6.0-Pt catalyst, dehydrogenation is less favorable because of the dominant exposure of WC sites on surface. Thus, despite exhibiting the same equilibrium position (dictated solely by the temperature and pressure of reaction) as the 0.4-Pt catalyst, product selectivity for the 6.0-Pt favors saturated ring species.

The most surprising conclusion resulting from the work described here is the structure sensitivity for dehydroxylation of phenolics facilitated by WC sites. This step is the most catalytically demanding, considering the C_{aryl}-OH bond is the strongest C-O bond present in lignin-derived phenolics[33], and thus it is surprising that our work identifies WC sites as critical for the cleavage of these C-O bonds, especially since C_{aryl}-OCH_3 bonds were cleaved by UC sites. In general, WC metal sites are regarded as less reactive than under-coordinated (UC) sites. Importantly, this trend holds over both DHE and PHE substrates at low and high conversions, supporting the conclusions discussed earlier that deactivation is not influencing structure sensitivity and that this behavior holds for diverse substrates.

In catalytic HDO schemes, the following pathways have been suggested for dehydroxylation of phenolics over metal catalysts: hydrogenation followed by dehydration[96-98], direct deoxygenation (DDO)[99-101], and tautomerization[58,91]. Complete

hydrogenation to a cyclohexanol intermediate followed by dehydration has been rejected previously for Pt/SiO_2 catalysts because of the inherent lack of acidity of the silica support, and will not be considered here further. DDO, or direct cleavage of the C_{aryl}-OH bond without any other mechanistic steps, has also been proposed as a pathway for HDO of phenolics. Typically, the DDO mechanism is invoked in systems involving oxophilic components. For instance, NiFe surfaces have been predicted by DFT to proceed through DDO[102]. However, over weakly oxophilic monometallic catalysts such as Pt/SiO_2, DDO is considered kinetically unfavorable under the conditions studied here. Additionally, UC sites are predicted to facilitate DDO more effectively, opposite the structure sensitivity observed in our reactions. Thus, DDO is an unlikely mechanism for our system.

Instead, we propose that the structure sensitivity observed here for the dehydroxylation of PHE to BNZ is consistent with a pathway involving metal-facilitated aromatic tautomerization. Tautomerization-based mechanisms for HDO have gained increased attention for a range of metal catalysts, specifically for non-acidic catalysts. The proposed mechanistic steps are shown in Scheme 5. Briefly, PHE is adsorbed to Pt and tautomerized to the corresponding 4-propylcyclohexa-3,5-dien-1-one (DiONE). The C=O bond in DiONE is then hydrogenated to form the unstable 4-propylcyclohexa-3,5-dien-1-ol (DiOL), which readily undergoes dehydration to form BNZ. Importantly, these tautomerization events are proposed to occur while the substrate is adsorbed to the metal catalyst surface, as tautomerization of phenol to the keto form in free solvent environments is negligible due to the favorable stability of the aromatic ring[103]. Thus, it might be expected that metal surface characteristics change the favorability of tautomerization.

The greater selectivity of 6.0-Pt towards BNZ and CYC from HDO of both DHE and PHE substrates is indicative of WC sites promoting tautomerization. We attribute this behavior to an adsorption effect which can proceed more readily over WC sites wherein phenolics adsorb co-planar with the metal surface prior to tautomerization, analogous to the adsorption mode required for hydrogenation. The shared need for co-planar ring adsorption between both hydrogenation and tautomerization pathways is consistent with the need to disrupt ring aromaticity in both reactions. On the other hand, UC sites on stepped surfaces or at particles edges do not exhibit the contiguous ensembles necessary to achieve intermediate stabilization. This would explain the inability of 0.4-Pt to produce significant quantities of BNZ or CYC, even at conditions of high conversion and high H_2 pressure. This would also explain the differences in selectivity between 0.4-Pt and 2.0-Pt in the HDO of PHE, as the hydrogenation of PHE is proposed to proceed through a tautomerization mechanism to produce ONE[104]. Considering the inability of 0.4-Pt to facilitate this tautomerization, the favored product is instead OL. This is consistent with the larger particle size of 2.0-Pt exhibiting more WC sites. On the other hand, similarity in performance between 0.4-Pt and 2.0-Pt in HDO of DHE is consistent with the initial demethoxylation step of DHE not involving tautomerization, but rather direct cleavage or demethylation to CAT.

Regarding the influence of the metal surface on tautomerization, there are few works which comment on the promotion or suppression of the tautomerization pathways for HDO. It is known that metal identity is critical in determining the dominant HDO pathway, with relatively oxophilic metals such as Ru favoring direct C-O cleavage[100], whereas Pt prefers tautomerization pathways[91]. However, the tendency of a specific metal to facilitate tautomerization has been shown to be sensitive to the electronic and compositional characteristics of the catalyst. For instance, bimetallic PtMo alloy catalysts promote tautomerization compared to monometallic Pt catalysts in HDO of *m*-cresol[91]. DFT calculations supported the hypothesis that the oxophilicity of Mo sites promote strong interactions with the keto tautomer, decreasing barriers of tautomerization. Similarly, alkali-modification of Fe catalysts for HDO resulted in the destabilization of tautomer intermediates depending on the degree of electron donation, demonstrating a relationship between metal electronics and tautomerization[17]. Given the relative similarity in electronic structure of Pt sites of varying coordination in our studies, we hypothesize that the reactant adsorption geometry on Pt sites is primarily responsible for the moderation of tautomerization of phenolic substrates such as DHE and PHE. However, we cannot rule out the potential contribution of electronic differences between UC and WC Pt sites in tautomerization reactions.

Conclusion

In conclusion, the directed synthesis of various sized Pt catalysts supported on SiO_2 enabled the assessment of structure sensitivity in HDO reactions. Importantly, by employing both DHE and PHE as substrates, we have shown that observed structure sensitivity trends exist for both mono-oxygenated and multi-oxygenated phenolics. Analysis of the products distribution provided the surprising result that larger Pt nanoparticles, in this case 12 nm in size, were superior to Pt nanoparticles <3 nm in catalyzing complete HDO of DHE and PHE to BNZ. Though this runs counter to the observation that DDO is facilitated over smaller nanoparticles, our results suggest that an alternative pathway, namely surface-mediated tautomerization of phenol to dienone, is responsible for full deoxygenation. This conclusion underscores the potential of facilitating tautomerization HDO pathways to enhance overall deoxygenation activity. These results also highlight the balance that exists for monometallic catalysts in which large particles drive rapid deoxygenation but with broad product distributions, compared to the slower but more selective HDO found for smaller Pt particles.

Author Contributions

JM: conceptualization, methodology, validation, formal analysis, investigation, data curation, visualization, writing – original draft, writing – review & editing. PCF: writing – review

& editing, supervision. MMAO: conceptualization, methodology, resources, data curation, writing – review & editing, supervision, funding acquisition, project administration. PC: conceptualization, methodology, resources, data curation, writing – review & editing, supervision, funding acquisition, project administration. All authors approved the final version of the manuscript.

Conflicts of Interest

MMAO is founder and part owner of Spero Renewables, LLC, a technology company focused on plant-based renewables. Activities with Spero have been disclosed to UCSB in accordance with UCSB's Policy on Conflict of Commitment and Outside Professional Activities.

Acknowledgements

This work was supported by the Catalysis Center for Energy Innovation, an Energy Frontier Research Center funded by the U.S. Department of Energy, Office of Science, Office of Basic Energy Sciences under Award No. DE-SC0001004. Electron microscopy was performed at the MRL Shared Experimental Facilities, which are supported by the MRSEC Program of the NSF under Award No. DMR 1720256; a member of the NSF-funded Materials Research Facilities Network (www.mrfn.org). P.C. and M.A.O. both acknowledge the Mellichamp Academic Initiative in Sustainability at UCSB for support.

Notes and references

1 Ragauskas, A. J. *et al.* The Path Forward for Biofuels and Biomaterials. *Science (1979)* **311**, 484–489 (2006).
2 Meng, Q. *et al.* Sustainable production of benzene from lignin. *Nat Commun* **12**, (2021).
3 Alherech, M. *et al.* From Lignin to Valuable Aromatic Chemicals: Lignin Depolymerization and Monomer Separation via Centrifugal Partition Chromatography. *ACS Cent Sci* **7**, 1831–1837 (2021).
4 Mruthyunjaya, V. Catalysis for bio-BTX (benzene, toluene, and xylene) synthesis. in *Advanced Catalysis for Drop-in Chemicals* 223–256 (Elsevier, 2021). doi:10.1016/B978-0-12-823827-1.00003-1.
5 Omran, H. R., EL-Marsafy, S. M., Ashour, F. H. & Abadir, E. F. Economic evaluation of aromatics production, a case study for financial model application in petrochemical projects. *Egyptian Journal of Petroleum* **26**, 855–863 (2017).
6 Sudarsanam, P. *et al.* Towards Lignin-Derived Chemicals Using Atom-Efficient Catalytic Routes. *Trends in Chemistry* vol. 2 898–913 Preprint at https://doi.org/10.1016/j.trechm.2020.07.011 (2020).
7 Mante, O. D. *et al.* Integration of catalytic fast pyrolysis and hydroprocessing: A pathway to refinery intermediates and 'drop-in' fuels from biomass. *Green Chemistry* **18**, 6123–6135 (2016).
8 Liu, C., Wang, H., Karim, A. M., Sun, J. & Wang, Y. Catalytic fast pyrolysis of lignocellulosic biomass. *Chemical Society Reviews* vol. 43 7594–7623 Preprint at https://doi.org/10.1039/c3cs60414d (2014).
9 Ma, Z., Troussard, E. & van Bokhoven, J. A. Controlling the selectivity to chemicals from lignin via catalytic fast pyrolysis. *Appl Catal A Gen* **423–424**, 130–136 (2012).
10 Jiang, G., Nowakowski, D. J. & Bridgwater, A. v. Effect of the temperature on the composition of lignin pyrolysis products. *Energy and Fuels* **24**, 4470–4475 (2010).
11 Bai, X. *et al.* Formation of phenolic oligomers during fast pyrolysis of lignin. *Fuel* **128**, 170–179 (2014).
12 van den Bosch, S. *et al.* Reductive lignocellulose fractionation into soluble lignin-derived phenolic monomers and dimers and processable carbohydrate pulps. *Energy Environ Sci* **8**, 1748–1763 (2015).
13 Galkin, M. V & Samec, J. S. M. Lignin Valorization through Catalytic Lignocellulose Fractionation:A Fundamental Platform for the Future Biorefinery. *ChemSusChem* **9**, 1544–1558 (2016).
14 Anderson, E. M. *et al.* Reductive Catalytic Fractionation of Corn Stover Lignin. *ACS Sustain Chem Eng* **4**, 6940–6950 (2016).
15 Lu, Q. *et al.* Ordered mesoporous metal carbides with enhanced anisole hydrodeoxygenation selectivity. *ACS Catal* **6**, 3506–3514 (2016).
16 Ren, H. *et al.* Selective hydrodeoxygenation of biomass-derived oxygenates to unsaturated hydrocarbons using molybdenum carbide catalysts. *ChemSusChem* **6**, 798–801 (2013).
17 Zhang, J. *et al.* Elucidating the Active Site and the Role of Alkali Metals in Selective Hydrodeoxygenation of Phenols over Iron-Carbide-based Catalyst. *ChemSusChem* **14**, 4546–4555 (2021).
18 Yu, Z. *et al.* Hydrodeoxygenation of phenolic compounds to cycloalkanes over supported nickel phosphides. *Catal Today* **319**, 48–56 (2019).
19 Bowker, R. H. *et al.* Synthesis and hydrodeoxygenation properties of ruthenium phosphide catalysts. *ACS Catal* **1**, 917–922 (2011).
20 Hsu, P. J. & Lin, Y. C. Hydrodeoxygenation of 4-methylguaiacol over silica-supported nickel phosphide catalysts: The particle size effect. *J Taiwan Inst Chem Eng* **79**, 80–87 (2017).
21 Jiang, G., Hu, Y., Xu, G., Mu, X. & Liu, H. Controlled Hydrodeoxygenation of Phenolic Components in Pyrolysis Bio-oil to Arenes. *ACS Sustain Chem Eng* **6**, 5772–5783 (2018).
22 Yang, Y. *et al.* Effect of metal-support interaction on the selective hydrodeoxygenation of anisole to aromatics over Ni-based catalysts. *Appl Catal B* **145**, 91–100 (2014).
23 Laskar, D. D., Tucker, M. P., Chen, X., Helms, G. L. & Yang, B. Noble-metal catalyzed hydrodeoxygenation of biomass-derived lignin to aromatic hydrocarbons. *Green Chemistry* **16**, 897–910 (2014).
24 Echeandia, S. *et al.* Enhancement of phenol hydrodeoxygenation over Pd catalysts supported on mixed HY zeolite and Al2O3. An approach to O-removal from bio-oils. *Fuel* **117**, 1061–1073 (2014).
25 Zhu, X., Nie, L., Lobban, L. L., Mallinson, R. G. & Resasco, D. E. Efficient conversion of m-cresol to aromatics on a bifunctional Pt/HBeta catalyst. *Energy and Fuels* **28**, 4104–4111 (2014).
26 Ji, N. *et al.* More than a support: the unique role of Nb2O5 in supported metal catalysts for lignin hydrodeoxygenation. *Catalysis Science and Technology* vol. 12 3751–3766 Preprint at https://doi.org/10.1039/d2cy00245k (2022).
27 Lee, C. R. *et al.* Catalytic roles of metals and supports on hydrodeoxygenation of lignin monomer guaiacol. *Catal Commun* **17**, 54–58 (2012).
28 Cordero-Lanzac, T. *et al.* Revealing the pathways of catalyst deactivation by coke during the hydrodeoxygenation of raw bio-oil. *Appl Catal B* **239**, 513–524 (2018).
29 Li, Y. *et al.* Coke formation on the surface of Ni/HZSM-5 and Ni-Cu/HZSM-5 catalysts during bio-oil hydrodeoxygenation. *Fuel* **189**, 23–31 (2017).

30 Wang, C. *et al.* Mechanistic Study of the Direct Hydrodeoxygenation of m -Cresol over WOx-Decorated Pt/C Catalysts. *ACS Catal* **8**, 7749–7759 (2018).
31 Martinez-Klimov, M. *et al.* Bifunctional Pt–Re Catalysts in Hydrodeoxygenation of Isoeugenol as a Model Compound for Renewable Jet Fuel Production. *ACS Engineering Au* **2**, 436–449 (2022).
32 Héroguel, F., Nguyen, X. T. & Luterbacher, J. S. Catalyst Support and Solvent Effects during Lignin Depolymerization and Hydrodeoxygenation. *ACS Sustain Chem Eng* **7**, 16952–16958 (2019).
33 Prasomsri, T., Shetty, M., Murugappan, K. & Román-Leshkov, Y. Insights into the catalytic activity and surface modification of MoO 3 during the hydrodeoxygenation of lignin-derived model compounds into aromatic hydrocarbons under low hydrogen pressures. *Energy Environ Sci* **7**, 2660–2669 (2014).
34 Saraeian, A., Burkhow, S. J., Jing, D., Smith, E. A. & Shanks, B. H. Catalyst Property Effects on Product Distribution during the Hydrodeoxygenation of Lignin Pyrolysis Vapors over MoO3/γ-Al2O3. *ACS Sustain Chem Eng* **9**, 6685–6696 (2021).
35 Murugappan, K. *et al.* Operando NAP-XPS unveils differences in MoO3 and Mo2C during hydrodeoxygenation. *Nat Catal* **1**, 960–967 (2018).
36 Ohta, H. *et al.* Low temperature hydrodeoxygenation of phenols under ambient hydrogen pressure to form cyclohexanes catalysed by Pt nanoparticles supported on H-ZSM-5. *Chemical Communications* **51**, 17000–17003 (2015).
37 Lee, W. S., Wang, Z., Wu, R. J. & Bhan, A. Selective vapor-phase hydrodeoxygenation of anisole to benzene on molybdenum carbide catalysts. *J Catal* **319**, 44–53 (2014).
38 Jia, X. & An, W. Adsorption of Monocyclic Aromatics on Transition Metal Surfaces: Insight into Variation of Binding Strength from First-Principles. *Journal of Physical Chemistry C* **122**, 21897–21909 (2018).
39 Ihm, H., Ajo, H. M., Gottfried, J. M., Bera, P. & Campbell, C. T. Calorimetric measurement of the heat of adsorption of benzene on Pt(111). *Journal of Physical Chemistry B* **108**, 14627–14633 (2004).
40 Campbell, J. M., Seimanides, S. & Campbell, C. T. Probing Ensemble Effects In Surface Reactions. 2. Benzene Adsorption on Clean and Bismuth-Covered Pt(111). *J. Phys. Chem* **93**, 815–826 (1989).
41 Flores, A. F., Burwell, R. L. & Butt, J. 8. *Structure Sensitivity of Benzene Hydrogenation on Supported Pt Catalysts*. *J. CHEM. SOC. FARADAY TRANS* vol. 88 (1992).
42 Liu, R. & An, W. Stepped M@Pt(211) (M = Co, Fe, Mo) single-atom alloys promote the deoxygenation of lignin-derived phenolics: Mechanism, kinetics, and descriptors. *Catal Sci Technol* **11**, 7047–7059 (2021).
43 Lu, J., Behtash, S., Mamun, O. & Heyden, A. Theoretical Investigation of the Reaction Mechanism of the Guaiacol Hydrogenation over a Pt(111) Catalyst. *ACS Catal* **5**, 2423–2435 (2015).
44 Chiu, C. C., Genest, A., Borgna, A. & Rösch, N. C-O cleavage of aromatic oxygenates over ruthenium catalysts. A computational study of reactions at step sites. *Physical Chemistry Chemical Physics* **17**, 15324–15330 (2015).
45 Resasco, J. *et al.* Relationship between Atomic Scale Structure and Reactivity of Pt Catalysts: Hydrodeoxygenation of m-Cresol over Isolated Pt Cations and Clusters. *ACS Catal* **10**, 595–603 (2020).
46 Mortensen, P. M., Grunwaldt, J. D., Jensen, P. A. & Jensen, A. D. Influence on nickel particle size on the hydrodeoxygenation of phenol over Ni/SiO2. *Catal Today* **259**, 277–284 (2016).
47 Yang, F. *et al.* Size Dependence of Vapor Phase Hydrodeoxygenation of m-Cresol on Ni/SiO2 Catalysts. *ACS Catal* **8**, 1672–1682 (2018).
48 Miller, J. T., Schreier, M., Kropf, A. J. & Regalbuto, J. R. A fundamental study of platinum tetraammine impregnation of silica: 2. The effect of method of preparation, loading, and calcination temperature on (reduced) particle size. *J Catal* **225**, 203–212 (2004).
49 Zakem, G., Ro, I., Finzel, J. & Christopher, P. Support functionalization as an approach for modifying activation entropies of catalytic reactions on atomically dispersed metal sites. *J Catal* **404**, 883–896 (2021).
50 Goguet, A., Schweich, D. & Candy, J. P. Preparation of a Pt/SiO2 catalyst: II. Temperature-programmed decomposition of the adsorbed platinum tetrammine hydroxide complex under flowing hydrogen, oxygen, and argon. *J Catal* **220**, 280–290 (2003).
51 Yoshinobu, J., Tsukahara, N., Yasui, F., Mukai, K., Yamashita, Y. Lateral Displacement Transient Mobility in Chemisorption of CO on Pt(997). *Phys. Rev. Letters.* **90**, 248301-4 (2003).
52 Hayden, B.E., Kretzschmar, K., Bradshaw, A.M., Greenler, R.G. An infrared study on the adsorption of CO on a stepped platinum surface. *Surf. Sci.* **149**, 394-406 (1985).
53 Kaneko, S. *et al.* Pt dispersion control in Pt/SiO 2 by calcination temperature using chloroplatinic acid as catalyst precursor. *Appl Catal A Gen* **427–428**, 85–91 (2012).
54 Scanlon, J. T. & Willis, D. E. *Calculation of Flame Ionization Detector Relative Response Factors Using the Effective Carbon Number Concept*. *Journal of Chromatographic Science* vol. 23 (1985).
55 Yieru, H., Qingyu, O. & Weile, Y. Characteristics of Flame Ionization Detection for the Quantitative Analysis of Complex Organic Mixtures. *Anal. Chem* **62**, 2063 (1990).
56 Holm, T. *Aspects of the mechanism of the flame ionization detector*. *Journal of Chromatography A* vol. 842 (1999).
57 Zhang, X., Tang, W., Zhang, Q., Wang, T. & Ma, L. Hydrocarbons Production from Lignin-derived Phenolic Compounds over Ni/SiO2 Catalyst. *Energy Procedia* **105**, 518–523 (2017).
58 Nie, L. & Resasco, D. E. Kinetics and mechanism of m-cresol hydrodeoxygenation on a Pt/SiO 2 catalyst. *J Catal* **317**, 22–29 (2014).
59 Ngandjong, A. C., Mottet, C. & Puibasset, J. Influence of the Silica Support on the Structure and the Morphology of Silver Nanoparticles: A Molecular Simulation Study. *Journal of Physical Chemistry C* **120**, 8323–8332 (2016).
60 Ma, Q., Klier, K., Cheng, H., Mitchell, J. W. & Hayes, K. S. Interaction between catalyst and support. 3: Metal agglomeration on the silica surface. *Journal of Physical Chemistry B* **105**, 9230–9238 (2001).
61 Ferreira-Aparicio, P., Rodriguez-Ramos, I. & Guerrero-Ruiz, A. *Methane interaction with silica and alumina supported metal catalysts*. *Applied Catalysis A: General* vol. 148 (1997).
62 Soled, S. Silica-supported catalysts get a new breath of life. *Science* vol. 350 1171–1172 Preprint at https://doi.org/10.1126/science.aad0267 (2015).
63 Agostini, G. *et al.* Determination of the particle size, available surface area, and nature of exposed sites for silica-alumina-supported Pd nanoparticles: A multitechnical approach. *Journal of Physical Chemistry C* **113**, 10485–10492 (2009).
64 Smith, J. S., Thrower, P. A. & Vannice, M. A. Characterization of Ni/TiO, Catalysts by TEM, X-Ray Diffraction, and Chemisorption Techniques. *J Catal* **68**, 270–285 (1981).
65 Kale, M. J. & Christopher, P. Utilizing Quantitative in Situ FTIR Spectroscopy to Identify Well-Coordinated Pt Atoms as the Active Site for CO Oxidation on Al2O3-Supported Pt Catalysts. *ACS Catal* **6**, 5599–5609 (2016).
66 Bergeret, G. & Gallezot, P. Particle Size and Dispersion Measurements. in *Handbook of Heterogeneous Catalysis* vol. 2 738–765 (Wiley-VCH, 2008).

67 Sangnier, A. *et al.* Thermokinetic and spectroscopic mapping of carbon monoxide adsorption on highly dispersed Pt/γ-Al2O3. *ACS Catal* **11**, 13280–13293 (2021).
68 Hayden, B. E., Bradshaw, A. M. & Greenler, R. G. AN INFRARED STUDY OF THE ADSORPTION OF CO ON A STEPPED PLATINUM SURFACE. *Surf Sci* **149**, 394–406 (1985).
69 Kappers, M. J. & Van Der Maas, J. H. *Correlation between CO frequency and Pt coordination number. A DRIFT study on supported Pt catalysts*. *Catalysis Letters* vol. 10 (1991).
70 Becker, E., Skoglundh, M., Andersson, M. & Spetz, A. L. In situ DRIFT study of hydrogen and CO adsorption on Pt/SiO2 model sensors. *IEEE Sensors* 1028–1031 (2007).
71 Brieger, C., Melke, J., Kaghazchi, P. & Roth, C. CO Adsorption on Platinum Nanoparticles - the Importance of Size Distribution Studied with in-Situ DRIFTS and DFT Calculations. *ECS Trans* **69**, 249–253 (2015).
72 Rioux, R. M. *et al.* Adsorption and co-adsorption of ethylene and carbon monoxide on silica-supported monodisperse Pt nanoparticles: Volumetric adsorption and infrared spectroscopy studies. *Langmuir* **24**, 198–207 (2008).
73 Podkolzin, S. G., Shen, J., De Pablo, J. J. & Dumesic, J. A. Equilibrated Adsorption of CO on Silica-Supported Pt Catalysts. *Journal of Physical Chemistry B* **104**, 4169–4180 (2000).
74 Woodruff, D. P., Hayden, B. E., Prince, K. & Bradshaw, A. M. *DIPOLE COUPLING AND CHEMICAL SHIFTS IN IRAS OF CO ADSORBED ON Cu(ll0)*. *Surface Science* vol. 123 (1982).
75 Kim, C. S., Tornquist, W. J. & Korzeniewskib, C. Site-dependent vibrational coupling of CO adsorbates on well-defined step and terrace sites of monocrystalline platinum: Mixed-isotope studies at Pt(335) and Pt(l11) in the aqueous electrochemical environment. *J. Chem. Phys.* **101**, 9113–9121 (1994).
76 Curulla, D., Clotet, A. & Ricart, J. M. Adsorption of carbon monoxide on Pt{100} surfaces: dependence of the CO stretching vibrational frequency on surface coverage. *Surf Sci* **460**, 101–111 (2000).
77 Choudary, V. R., Banerjee, S., Panjala, D. Influence of Temperature on the Product Selectivity and Distribution of Aromatics and C8 Aromatic Isomers in the Conversion of Dilute Ethene over H-Galloaluminosilicate (ZSM-5 type) Zeolite. *J. Catal.* **205**, 398-403 (2002).
78 Baharudin, K. B., Arumugam, M., Hunns, J., Lee, A. F., Mayes, E., Taufiq-Yap, Y. H., Wilson, K., Derawi, D. Octanoic acid hydrodeoxygenation over bifunctional Ni/Al-SBA-15 catalysts. *Catal. Sci. Technol.* **9**, 6673-6680 (2019).
79 Meunier, F. C., Yasmeen, A., Ross, J. R. H. Oxidative dehydrogenation of propane over molybdenum-containing catalysts. *Catal. Today.* **37**, 33-42 (1997).
80 De Souza, P. M. *et al.* Hydrodeoxygenation of Phenol over Pd Catalysts. Effect of Support on Reaction Mechanism and Catalyst Deactivation. *ACS Catal* **7**, 2058–2073 (2017).
81 Bykova, M. V., Zavarukhin, S. G., Trusov, L. I. & Yakovlev, V. A. Guaiacol hydrodeoxygenation kinetics with catalyst deactivation taken into consideration. *Kinetics and Catalysis* **54**, 40–48 (2013).
82 Lan, X., Hensen, E. J. M. & Weber, T. Hydrodeoxygenation of guaiacol over Ni2P/SiO2–reaction mechanism and catalyst deactivation. *Appl Catal A Gen* **550**, 57–66 (2018).
83 Huang, X., Koranyi, T. I., Boot, M. D., Hensen, E. J. M. Ethanol as capping agent and formaldehyde scavanger for efficient depolymerization of lignin to aromatics. *Green Chem.* **17**, 4941-4950 (2015).
84 Lindfors, C. Hydrodeoxygenation of lignin-derived phenol compound isoeugenol over nickel- and cobalt-based catalysts. [Unpublished master's thesis] Abo Akademi University. Turku, Finland (2019).
85 Tueli, S., Maki-Arvela, P., Peurla, M., Eranen, K., Warna, J., Cruciani, G., Menegazzo, F., Murzin, D. Y., Signoretto, M. Hydrodeoxygenation of isoeugenol over Ni-SBA-15: Kinetics and modelling. *Appl. Cat. A.* **580**, 1-10 (2019).
86 Bartolomei, E., Le Brech, Y., Dufour, A., Carre, V., Aubriet, F., Terrel, E., Garica-Perez, M., Arnoux, P. Lignin Depolymerization: A Comparison of Methods to Analyze Monomers and Oligomers. *ChemSusChem.* **13**, 4633-4648 (2020).
87 Le Valant, A. *et al.* Platinum supported catalysts: Predictive CO and H2 chemisorption by a statistical cuboctahedron cluster model. *Journal of Physical Chemistry C* **120**, 26374–26385 (2016).
88 Lin, S. D. & Vannice, M. A. Hydrogenation of Aromatic Hydrocarbons over Supported Pt Catalysts III. Reaction Models for Metal Surfaces and Acidic Sites on Oxide Supports. *J Catal* **143**, 563–572 (1993).
89 Gao, D., Xiao, Y. & Varma, A. Guaiacol Hydrodeoxygenation over Platinum Catalyst: Reaction Pathways and Kinetics. *Ind Eng Chem Res* **54**, 10638–10644 (2015).
90 Tan, Q. *et al.* Different Product Distributions and Mechanistic Aspects of the Hydrodeoxygenation of m-Cresol over Platinum and Ruthenium Catalysts. *ACS Catal* **5**, 6271–6283 (2015).
91 Robinson, A. *et al.* Enhanced Hydrodeoxygenation of m-Cresol over Bimetallic Pt-Mo Catalysts through an Oxophilic Metal-Induced Tautomerization Pathway. *ACS Catal* **6**, 4356–4368 (2016).
92 Rioux, R. M., Hsu, B. B., Grass, M. E., Song, H. & Somorjai, G. A. Influence of particle size on reaction selectivity in cyclohexene hydrogenation and dehydrogenation over silica-supported monodisperse pt particles. *Catal Letters* **126**, 10–19 (2008).
93 K G, L., Puthiyaparambath, M. F., S, A. & Chatanathodi, R. Adsorption of benzene on defective Pt surfaces: A DFT study. *Surf Sci* **716**, (2022).
94 Chen, T. & Vohs, J. M. Direct Hydrodeoxygenation of m-Cresol to Toluene over Bifunctional NbOx-Pt. *Journal of Physical Chemistry C* **124**, 14253–14261 (2020).
95 Gupta, S., Khan, T. S., Saha, B. & Haider, M. A. Synergistic Effect of Zn in a Bimetallic PdZn Catalyst: Elucidating the Role of Undercoordinated Sites in the Hydrodeoxygenation Reactions of Biorenewable Platforms. *Ind Eng Chem Res* **58**, 16153–16163 (2019).
96 Hočevar, B., Grilc, M. & Likozar, B. Aqueous dehydration, hydrogenation, and hydrodeoxygenation reactions of bio-based mucic acid over ni, nimo, pt, rh, and ru on neutral or acidic catalyst supports. *Catalysts* **9**, (2019).
97 Zhao, C., He, J., Lemonidou, A. A., Li, X. & Lercher, J. A. Aqueous-phase hydrodeoxygenation of bio-derived phenols to cycloalkanes. *J Catal* **280**, 8–16 (2011).
98 Zhao, C., Song, W. & Lercher, J. A. Aqueous phase hydroalkylation and hydrodeoxygenation of phenol by dual functional catalysts comprised of Pd/C and H/La-BEA. *ACS Catal* **2**, 2714–2723 (2012).
99 Nelson, R. C. *et al.* Experimental and Theoretical Insights into the Hydrogen-Efficient Direct Hydrodeoxygenation Mechanism of Phenol over Ru/TiO2. *ACS Catal* **5**, 6509–6523 (2015).
100 Bui, V. N., Laurenti, D., Afanasiev, P. & Geantet, C. Hydrodeoxygenation of guaiacol with CoMo catalysts. Part I: Promoting effect of cobalt on HDO selectivity and activity. *Appl Catal B* **101**, 239–245 (2011).
101 Wang, S. *et al.* Hydrodeoxygenation of anisole to benzene over an Fe2P catalyst by a direct deoxygenation pathway. *Catal Sci Technol* **10**, 3015–3023 (2020).
102 Liu, X., An, W., Turner, C. H. & Resasco, D. E. Hydrodeoxygenation of m-cresol over bimetallic NiFe alloys: Kinetics and thermodynamics insight into reaction mechanism. *J Catal* **359**, 272–286 (2018).

103 Capponi, M., Gut, I. G., Hellrung, B., Persy, G. & Wirz, J. Ketonization equilibria of phenol in aqueous solution 1. *Can. J. Chem.* **77**, 605–613 (1999).

104 Chen, H., Sun, J., Selective hydrogenation of phenol for cyclohexanone: A review. *J. Ind. Eng. Chem.* **94**. 78-91 (2021).